RSC Advances

ROYAL SOCIETY OF CHEMISTRY

PAPER

View Article Online
View Journal | View Issue

Cite this: *RSC Adv.*, 2025, **15**, 33976

Selective adsorption of Pb(II) on green Sn-BDC-MOF/GO composite: optimization, DFT studies and mechanism

Mohamed Fouad,*[a] Gehan M. El-Subruiti,[a] Ahmed Hasanein[a] and Abdelazeem Eltaweil *[ab]

Received 9th July 2025
Accepted 10th September 2025

DOI: 10.1039/d5ra04912a

rsc.li/rsc-advances

Scientists have made significant strides in removing heavy metals like lead (Pb(II)) from water, recognizing their adverse effects on human health. A new, eco-friendly composite material, Tin-benzene dicarboxylic acid metal organic framework/graphene oxide (Sn-BDC-MOF/GO), has been developed for this purpose. This material was meticulously analyzed using various chemical, textural, and structural techniques to confirm its effective creation. Through experiments, it was found that Sn-BDC-MOF/GO efficiently removes Pb(II) ions at 25 °C and a pH of 6, following a second-order kinetic model. The adsorption capacity reached a maximum of 200.0 mg g^{-1}, suggesting both chemical and physical adsorption processes as evidenced by Langmuir and Freundlich isotherm models. Thermodynamic analysis showed that adsorption is orderly, exothermic, and spontaneous. Furthermore, we examined the effect of interfering ions on the composite's affinity, demonstrating excellent selectivity toward Pb(II) ions and good recyclability over six cycles. Advanced spectroscopic methods, Density Functional Theory (DFT), and Monte Carlo simulations provided deep insights into the adsorption mechanism, particularly the electronic structure and intermolecular interactions. DFT calculations pinpointed the most effective adsorption sites and estimated significant adsorption energies, enhancing our understanding of the molecular-level adsorption process. This study not only advances our knowledge in creating efficient adsorbents for heavy metal removal from water but also emphasizes the crucial role of DFT in understanding and optimizing adsorption mechanisms.

1 Introduction

Water pollution, affecting both human and wildlife health, manifests as a pressing concern in today's world due to its significant impacts on public health and ecological stability.[1,2] Heavy metals are widely recognized as the most perilous form of pollutants because of their extreme toxicity, remarkable persistence, and tendency to accumulate in the environment for extended periods.[3] They can penetrate the environment through several channels, including volcanic eruptions, the erosion of rocks that harbor heavy metals, human actions such as mining, agriculture, and mineral extraction, as well as diverse industrial procedures.[4] Contaminated water containing heavy metals, including lead, cadmium, mercury, and arsenic, poses an extreme and immediate threat to public health.[5]

Lead ions are known to be the most harmful and hazardous heavy metal found in the environment, an issue dating back to historical times due to its significant physicochemical properties. Despite being widespread, lead poses significant and hazardous environmental risks globally. Its usage is challenging to curb due to its unique properties such as softness, ductility, malleability, weak conductivity, and resistance to corrosion. As a result, it remains a non-biodegradable metal and continues to be used, leading to an increase in its concentration in the environment, which in turn poses significant risks.[6] Water can become contaminated with lead from several sources, including plumbing fixtures, faucets, and lead pipes. Additionally, industrial processes like lead smelting, combustion, ceramics, lead-based painting, battery recycling, pigments, and book printing may also contribute to lead contamination in water.[7] Lead is a dangerous substance that can accumulate in the human body and cause harm to essential organs like the brain, liver, kidneys, heart, and bones. Even the presence of tiny amounts of lead in water can pose significant health risk. Exposure to Pb(II) can result in autoimmune diseases, where the immune system attacks healthy cells by mistake, resulting in conditions like rheumatoid arthritis, nervous system disorders, and kidney disease. Kids are especially vulnerable to lead poisoning, which can negatively impact their growth and development, lower their IQ, or even lead to fatalities.[8]

---

[a] *Chemistry Department, Faculty of Science, Alexandria University, Alexandria, Egypt. E-mail: Mohamed.afouad@alexu.edu.eg; gehanmsubruiti@alexu.edu.eg; ahmedhasanein@alexu.edu.eg; abdelazeemeltaweil@alexu.edu.eg*

[b] *Department of Engineering, College of Engineering and Technology, University of Technology and Applied Sciences, Sultanate of Oman*

Numerous methods have been devised to eliminate lead ions from water, including ion exchange method, membrane filtration for lead, lead precipitation by chemical method, liquid extraction, and electro-dialysis. Unfortunately, these techniques can be quite costly, rendering them unsuitable for use by small-scale businesses. As a result, it is strongly advised that low-cost adsorbents be utilized in industrial wastewater treatment. These adsorbents are easily obtainable, sustainable, and economical, making them an optimal solution for engineering purposes.[9] In the water treatment process, a wide range of adsorbent materials are employed, including activated carbon, clays, carbon nanotubes, resin, and activated diatomite. It is crucial to ensure that water is completely free from any impurities and contaminants.[10] However, these adsorbents had some drawbacks including poor selectivity, challenging regeneration, low adsorption capacity, and complex production methods.[11]

Metal–organic frameworks (MOFs) are undisputed pioneers in water treatment. These highly porous crystalline materials are composed of metal ions or clusters that are bonded with organic linkers. Through extremely strong bonds.[12,13] Due to their intrinsic structural characteristics, including low densities, appreciably large surface areas, ease of tenability, and changeable pores, these kinds of materials have large-scale applications[14] such as gas storage,[15] adsorption,[16] catalysis,[17,18] drug delivery,[19] supercapacitors[20] and batteries.[21] The instability of MOFs in aqueous solutions is primarily due to the hydrolysis of the metal-linker coordination bond, which is caused by the hydrophilic nature of the metal nodes. This phenomenon can significantly disrupt the framework structure and must be considered when designing and utilizing MOFs in aqueous solutions.[22]

Another adsorbent material that has high efficiency in the adsorption process is GO, which is obtained from graphene which undergoes oxidation to become rich in oxygen-functional groups (such as carbonyl groups).[23] With its large surface area, high negative charge density and high adsorption capacity, it effectively removes metal ions.[24] Combining graphene oxide (GO) with MOF to coordinate the oxygen-containing functional groups of GO (–OH, –COOH, –C–O–C, and –C=O) with the metal centers of the MOF is a proven method to significantly enhance the properties of MOF.[25] This combination increases the stability of MOF in water due to preventing the adsorption of water by creating a hydrophobic barrier with carbon rings. Also, it raises the surface area of MOF and enhances the adsorption capacity.[26]

In our dedicated effort to develop environmentally sustainable materials, we have green synthesized the novel Sn-BDC-MOF/GO composite, which plays a pivotal role in environmental remediation by effectively removing lead ions from water. This advanced material combines the high surface area and customizable porosity of metal–organic frameworks (MOFs) with the superior adsorption capabilities graphene oxide (GO). The synergy between Sn-BDC-MOF and GO enhances the composite's stability and adsorption efficiency, making it highly effective in capturing lead ions from polluted water sources. (i) We characterized the physicochemical properties of the Sn-BDC-MOF/GO composite using XPS, XRD, FTIR, SEM, BET, and zeta potential (ZP) analyses. (ii) The adsorption capacity of the composite was evaluated in the lead adsorption process. (iii) Kinetic, isotherm, and thermodynamic studies were conducted on the experimental data to identify the interaction between Pb(II) and Sn-BDC-MOF/GO. (iv) Post-adsorption XPS analysis of Pb(II) was used to propose the controlled mechanisms within the Pb(II)/Sn-BDC-MOF/GO system. (v) A cycling test was performed over six runs to ensure the renewability of the Sn-BDC-MOF/GO composite. (vi) Furthermore, we employed Density Functional Theory (DFT) to elucidate the adsorption mechanisms of Pb(II) ions on the composite surface. This approach provided a comprehensive understanding of the electronic structures of both the adsorbates and adsorbents, enabling us to predict the nature of their interactions. Additionally, DFT allowed us to calculate adsorption energies, charge distributions, and the characteristics of the chemical bonds formed during the adsorption process. Moreover, DFT calculations were employed to validate the experimental data on the selectivity of the composite toward Pb(II) ions in the adsorption process. This detailed analysis is crucial for optimizing the material's performance in removing lead ions from water.

2 Experimental

2.1 Materials utilized

Stannous chloride dihydrate ($SnCl_2 \cdot 2H_2O$, 99.99%), terephthalic acid (H_2BDC-98%), sodium hydroxide (NaOH, 98%), and hydrogen peroxide (H_2O_2, 30%) were obtained from Sigma-Aldrich (Germany). Graphite powder, anhydrous sodium nitrate ($NaNO_3$, 99%), and sulfuric acid (H_2SO_4, 95–97%) were purchased from Loba Chemie (India). Anhydrous lead nitrate ($Pb(NO_3)_2$, 99%), potassium permanganate ($KMnO_4$, ≥99.0%) and were obtained from Alfa-Aesar Co. (UK).

2.2 Synthesis of green Sn-BDC MOF

The Sn-BDC MOF was created by deprotonating the carboxylic groups of 1.0 mmol of BDC with 2.0 mmol of NaOH. After combining the resulting mixture with 10 mL of distilled water and sonication for 15 min, a solution of 1.0 mmol of $SnCl_2 \cdot 2H_2O$ in 5 mL of distilled water was gradually added to the suspension solution of BDC, resulting in an intense milky solution. This solution was transferred to a 25 mL Teflon-lined stainless-steel autoclave, sealed tightly, and heated in an oven at 120 °C for 24 h. The pale-yellow powder precipitate was washed twice with distilled water and thrice with methanol using centrifugation at 7000 rpm for 5 min, then dried in an oven at 80 °C for 3 h. The yield of the product was 60% based on precursor salt.

2.3 Synthesis of graphene oxide

The process of synthesizing graphene oxide involves the utilization of Hummers' method. First, graphite powder weighing 1 g is combined with 80 mL of 98% concentrated H_2SO_4, followed by the addition of 0.5 g of $NaNO_3$ while constantly stirring at a low temperature of 4 °C. 5 g of $KMnO_4$ is then added, and stirring is continued for an additional 1 h. The solution is heated to 45 °C and maintained at this temperature for 40 min. Gradually, 100 mL of distilled water is added to the solution while heating it at 95 °C for 2 h. The process is completed by adding 300 mL of distilled water and 20 mL of 30% hydrogen peroxide to the reaction mixture. The resulting brown product is washed thrice with 10% HCl and thrice with distilled water through centrifugation at 7000 rpm for 3 min before being dried in an oven at 50 °C.

2.4 Synthesis of Sn(II)-MOF/GO composite

To create the Sn-BDC-MOF/GO composite, the calculated mass ratios of Sn MOF and GO were soaked in 20 mL of distilled water and sonicated the mixture for 30 min until a uniform binary suspension of Sn-BDC-MOF/GO was achieved. We then isolated the Sn-BDC-MOF/GO composite through centrifugation for 5 min and dried it for 12 h at 60 °C. Three different composites of mass ratios of Sn-BDC-MOF : GO were prepared as follow; Sn-BDC-MOF : GO (1 : 1), Sn-BDC-MOF : GO (3 : 1), and Sn-BDC-MOF : GO (1 : 3). The obtained materials were thoroughly characterized using a variety of tools, which are listed in the SI (Text S1).

2.5 Adsorption studies

In order to perform the experiment, a precisely measured amount of dry Sn-BDC-MOF/GO composite ranging from 0.005 to 0.02 g was introduced into a 20 mL water solution containing 50–200 mg L^{-1} of Pb(II) ions. The pH of the solution was then adjusted between 2 to 8 with the use of 0.1 M HCl and NaOH solutions. The experiment was conducted at a consistent shaking rate of 50 rpm while temperature varied from 298 to 328 K. At specific time intervals (1, 5, 10, 15, 30, 45, 60, 75, 90, and 115 min), the concentration of Pb(II) ions was measured at 217 nm using Atomic Absorption Spectroscopy (AAS) and the removal percentage (R%) of lead ions and adsorption capacity (q_t; mg g^{-1}) of the Sn-BDC-MOF/GO composite were calculated using the relevant eqn (1) and (2).

$$R\% = \frac{C_0 - C_t}{C_0} \times 100 \tag{1}$$

$$q_t = \frac{(C_0 - C_t) \times V}{m} \tag{2}$$

C_0 and C_t (mg L^{-1}) represents the concentration of lead ions (mg L^{-1}) at time zero and certain time. V(L) refers to the volume solution of lead ions and m (g) refers to the mass of Sn-BDC-MOF/GO composite.

2.6 Reusability studies

To evaluate the Sn-BDC-MOF/GO composite's reusability, six adsorption/desorption cycles were conducted. The composite effectively adsorbed lead ions and was easily separated *via* centrifugation. The desorption process was carried out using 0.2 M HCl, and the resulting mixture was shaken on a rotary shaker for 30 min at 200 rpm. After elution, the composite was rinsed thrice with distilled water to eliminate any residual acid. The composite was dried by using an air oven at 60 °C for 3 h before the next adsorption experiment.

3 Results and discussions

3.1 Characterization of the adsorbent material

3.1.1 FTIR. The FTIR spectra depicted in Fig. 1A highlights the GO, Sn-BDC MOF, and Sn-BDC-MOF/GO composite. Regarding GO, the stretching vibration peaks at 3350, 1720, 1614, 1371, and 1043 cm^{-1} are assigned to O–H, C=O, C=C (aromatic ring), C–OH, and C–O (epoxy) bonds,[27,28] respectively. In the case of Sn-BDC-MOF, the observed characteristic peak at ~580 cm^{-1},[29,30] is attributed to Sn–O stretching vibration. The peaks at 3440, 1689, 945, and 779 cm^{-1} can be attributed to the O–H, C=O, and C–H stretching vibrations, respectively.[31] Additionally, peaks at 1509 and 1570 cm-1 due to asymmetrical vibrations (COO^-), and at 1286 and 1423 cm^{-1} for symmetrical vibrational of (COO^-)[32] are also observed. The Sn-BDC-MOF/GO composite exhibits all characteristic peaks of both GO and Sn-BDC-MOF, indicating successful synthesis. Furthermore, all peaks are sharper than Sn-BDC-MOF, which confirms the combination achieved between MOF and GO.[31,33]

3.1.2 XRD. Fig. 1B highlights a notable peak at $2\theta = 10.25°$ in the X-ray diffraction pattern of GO.[34] The significant peaks of Sn-BDC-MOF at $2\theta = 9.09°$, 25.27°, 26.5°, 27.93°, and 33.78° are consistent with those of Sn-BDC-MOF, establishing the crystalline nature of MOF.[35–39] Moreover, it can be observed that the Sn-MOF/GO composite has similar characteristic peaks of parent Sn-BDC-MOF, but the peaks have lower intensities after modification with GO which indicates that the composite was successfully fabricated.

3.1.3 Zeta potential (ZP) measurements. The Sn-BDC-MOF/GO composite's point of zero charge (pH_{PZC}) was identified through zeta potential (ZP) measurement. At this point, the surface net charge of the composite becomes neutral. Below pH_{PZC}, the composite carries a positive charge, while it carries a negative charge at pH levels above pH_{PZC}.[40] The ZP measurement, depicted in Fig. S1, confirmed that the pH_{PZC} for Sn-BDC-MOF/GO composite is 2.8. This finding suggests that the composite can efficiently electrostatically adsorb metal ions at pH levels above 2.8. Moreover, the ZP of the composite decreased as the pH increased, leading to the deprotonation of the –COO– groups. At pH 6 and 8, the ZP decreased to −25.8 and −30.1 mV, respectively, thereby increasing the electrostatic attraction between the composite and Pb(II) ions at high pH levels.

3.1.4 XPS. According to the XPS survey in Fig. 2A, the Sn-BDC-MOF/GO composite consists of C 1s, Sn 3d, and O 1s elements, with corresponding binding energies (BE) of 286.16 eV, 488.19 eV, and 533.23 eV, respectively. Fig. 2B shows the O 1s curve, which exhibits characteristic peaks for M–O–C and O–C at binding energies of 531.97 eV and 533.09 eV, respectively.[41,42] Furthermore, the C 1s curve in Fig. 2C displays peaks at 284.49 eV, 285.95 eV, 286.84 eV, and 288.15 eV, corresponding to C=C, C–O, C=O, and O–C=O, respectively.[43] Finally, the Sn 3d spectrum in Fig. 2D suggests the presence of both Sn^{2+} and Sn^{4+}; Sn^{2+} displays distinctive peaks at binding

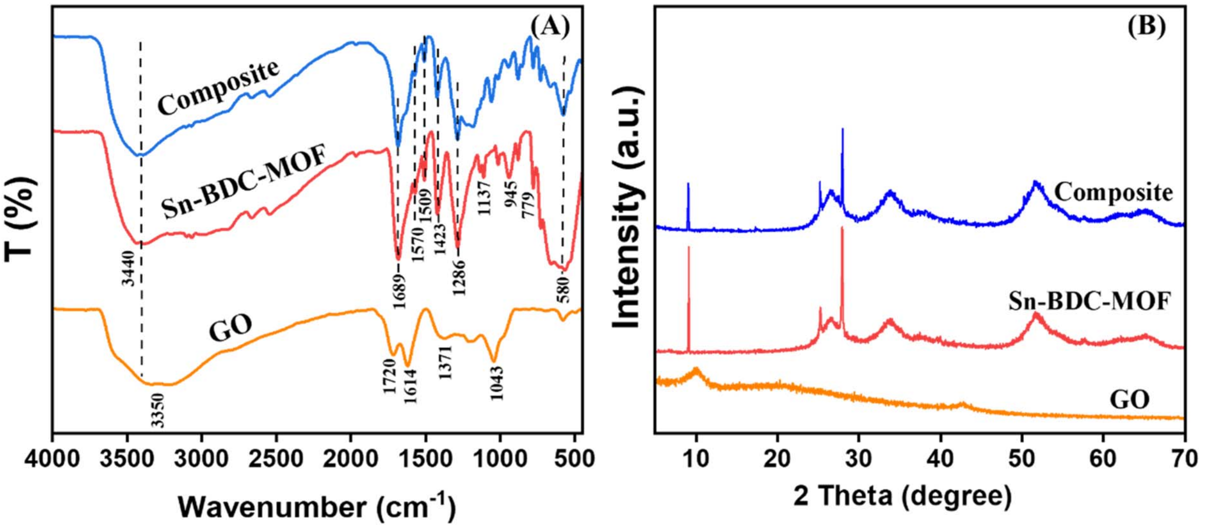

Fig. 1 (A) FTIR and (B) XRD for GO, Sn-BDC-MOF, and Sn-BDC-MOF/GO composite.

energies of 487.34 eV and 495.76 eV, while Sn^{4+} exhibits peaks at 487.75 eV and 495.8 eV.[44,45]

3.1.5 SEM. In Fig. 3A, SEM images revealed that Sn-BDC-MOF had irregular rod-like particle morphology. On the other hand, Fig. 3B showed GO with crumpled sheet-like morphology. It is clear from Fig. 3C that the irregular rod-like particles of Sn-BDC-MOF are well dispersed over the GO sheets, which significantly increases their adsorption capacity.

3.1.6 BET. Based on the findings presented in Fig. 4A and B, it is evident that both Sn-BDC-MOF and Sn-BDC-MOF/GO composite possess a mesoporous structure, as indicated by the IV-type isotherm with hysteresis loop H3-type. The BET surface area of Sn-BDC-MOF/GO is greater, measuring at 235.48

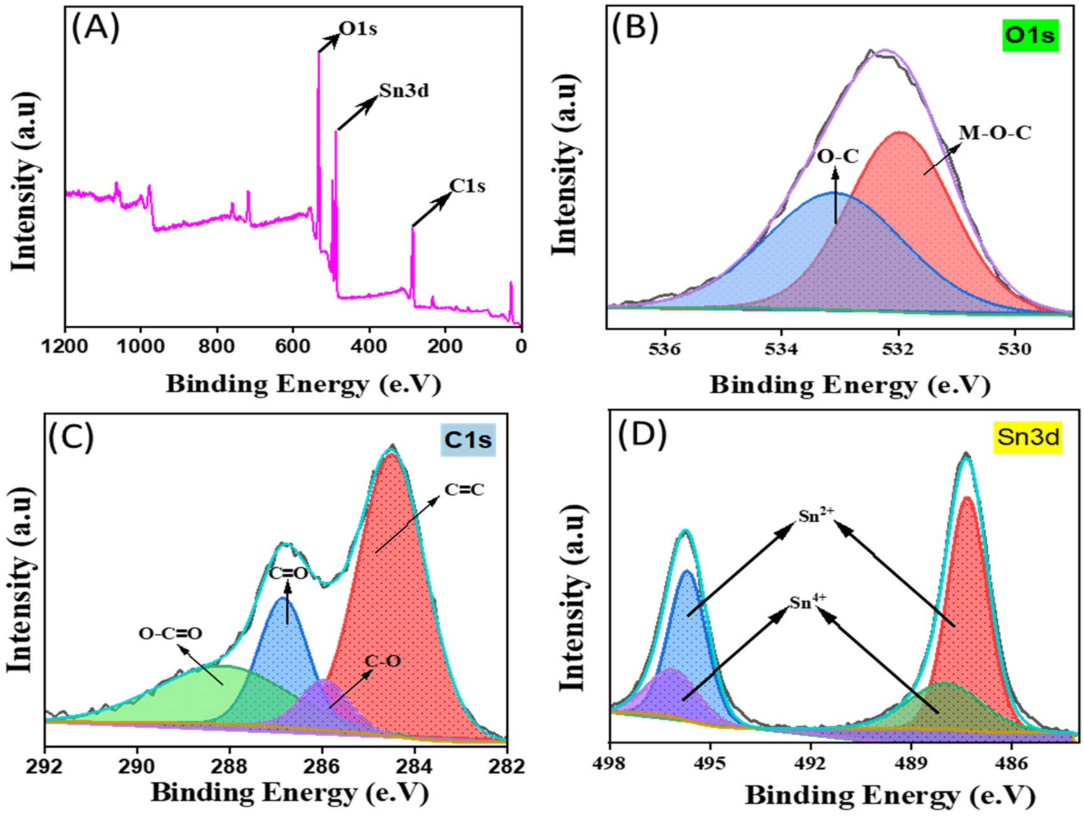

Fig. 2 XPS of Sn-BDC-MOF/GO composite before adsorption: (A) wide spectra, (B) O 1s, (C) C 1s, and (D) Sn 3d.

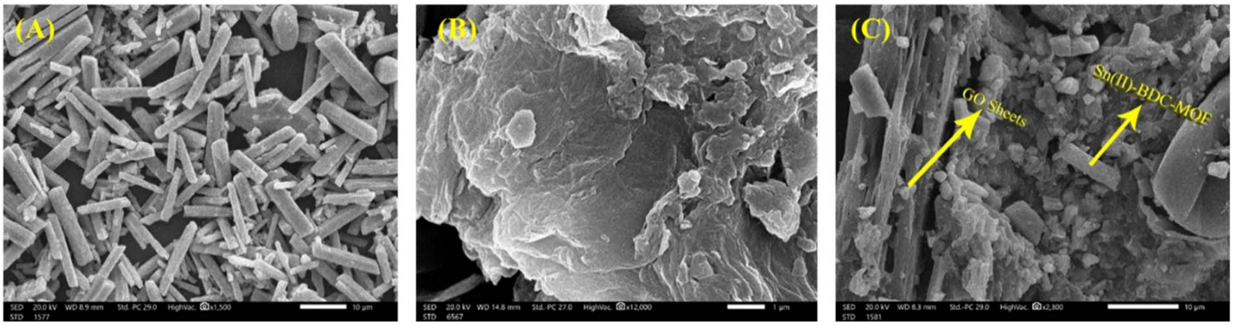

Fig. 3 SEM of (A) Sn-BDC-MOF, (B) GO, and (C) Sn-BDC-MOF/GO composite.

$m^2\,g^{-1}$, while Sn-BDC-MOF has a BET surface area of 148.96 $m^2\,g^{-1}$. The pore volumes of Sn-BDC-MOF/GO and Sn-BDC-MOF are 0.18 $cm^3\,g^{-1}$ and 0.10 $cm^3\,g^{-1}$, respectively. These observations suggest that the inclusion of GO enhances the surface area of Sn-BDC-MOF, ultimately making the adsorption process more efficient.

3.2 Factors affecting the adsorption process

3.2.1 The impact of pH. The adsorption process is significantly influenced by the pH level, which modifies the surface charges of the adsorbent and consequently impacts its adsorption capacity. To evaluate the adsorption of Pb(II), experiments were conducted across a pH range of 2.0 to 8.0. These experiments utilized 5 mg of the Sn-BDC-MOF/GO composite in 20 mL of Pb(II) solution, with an initial concentration of 50 mg L^{-1}, at a temperature of 25 °C for 60 min. As shown in Fig. 5A, an increase in pH results in an increase in both adsorption capacity and removal percentage. At lower pH levels, the Sn-BDC-MOF/GO composite surface becomes protonated, which makes the adsorption of Pb(II) more difficult.[31] Conversely, at higher pH levels, functional oxygen groups, such as carboxyl groups, become deprotonated, creating a greater negative charge on the composite surface which leads to an electrostatic attraction with positively charged Pb(II) ions.[46] This observation is further substantiated by the zeta potential value of −25.8 mV at pH 6, where the highest removal percentage of 86.41% and an adsorption capacity of 69.13 mg g^{-1} were recorded. This indicates a strong electrostatic attraction between the composite surface and lead ions at this pH level. However, at pH levels exceeding 6.0, the adsorption process can become more complex due to the formation of $Pb(OH)_2$, as observed by Feng.[47]

3.2.2 The impact of adsorbent dosage. Fig. 5B illustrates the effect of different quantities of dry Sn-BDC-MOF/GO composite (0.005, 0.01, 0.015, and 0.02 g) on the adsorption of Pb(II) ions. The experiments were conducted using 20 mL of a Pb(II) ion solution with an initial concentration of 50 mg L^{-1}, at a pH of 6 and a temperature of 25 °C for 60 min. The results highlight that adjusting the composite amount significantly impacts adsorption capacity, offering essential insights for optimizing dosage to enhance lead ion removal from water. As the adsorbent dose increased from 0.005 to 0.02 grams, the removal efficiency improved from 75.31% to 96.11%, due to the increased availability of surface sites for Pb(II) ion adsorption. Conversely, the adsorption capacity of Pb(II) ions per unit mass of Sn-BDC-MOF/GO composite decreases to 38.44 mg g^{-1} when the adsorbent dose is increased to 0.02 g. This reduction in performance can be attributed to the overcrowding of composite particles.[48]

3.2.3 The impact of composite ratio. Our study aimed to evaluate the adsorption efficiency of Sn-BDC-MOF, GO, and

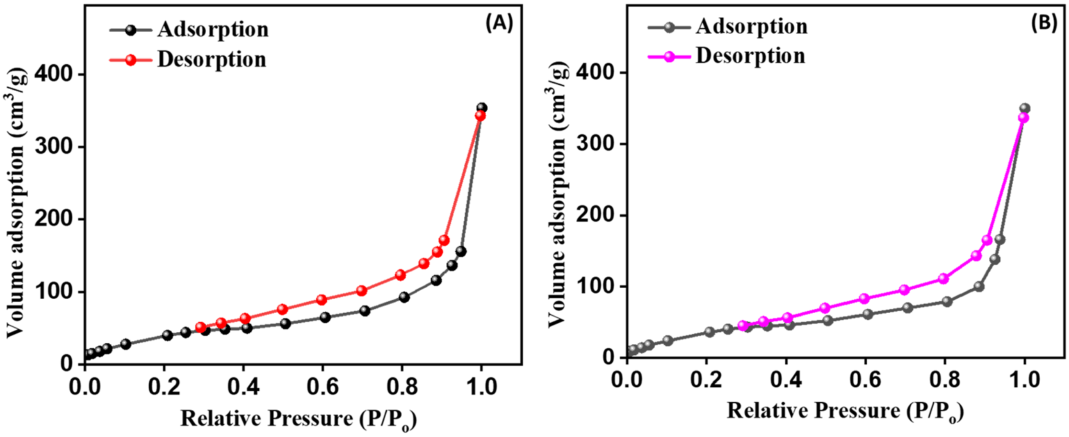

Fig. 4 N_2 adsorption–desorption isotherms of (A) Sn-BDC-MOF, (B) Sn-BDC-MOF/GO.

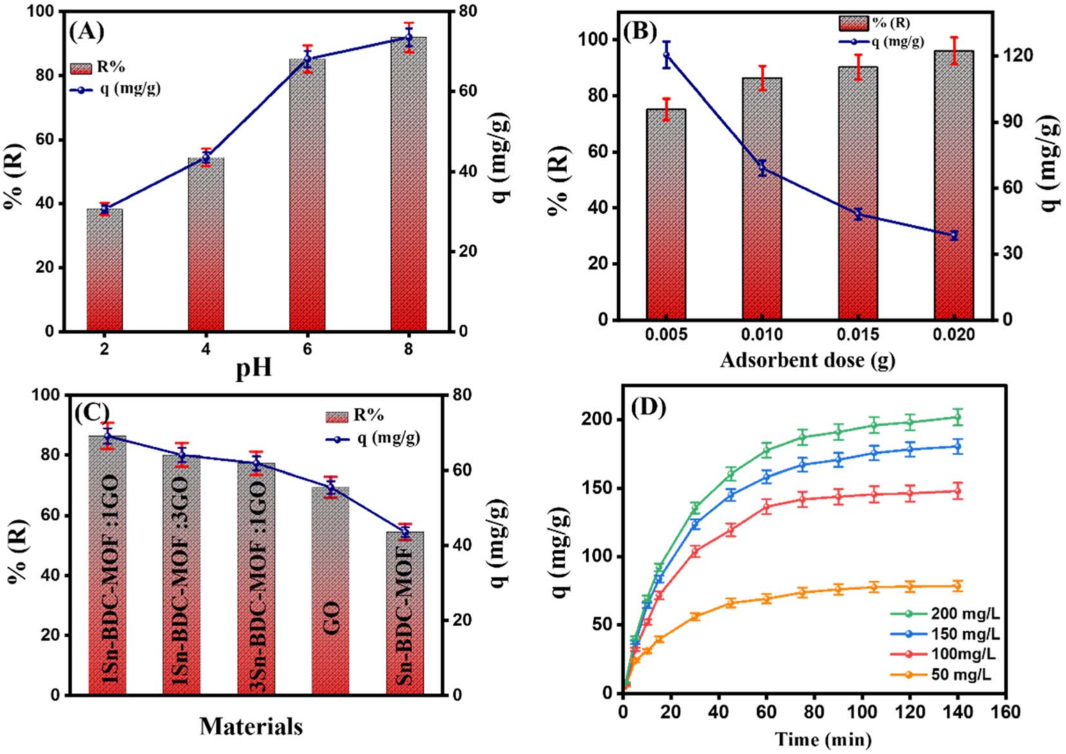

Fig. 5 Optimization of the Pb(II) adsorption onto Sn-BDC-MOF/GO; (A) pH, (B) dosage of Sn-BDC-MOF/GO, (C) composite ratio, and (D) initial concentration of Pb(II).

various ratios of the Sn-BDC-MOF/GO composite for the adsorption of Pb(II) ions. As illustrated in Fig. 5C, the adsorption capacities for the different ratios of the Sn-BDC-MOF/GO composite (1MOF : 1GO, 1MOF : 3GO, and 3MOF : 1GO), GO, and Sn-BDC-MOF were 69.12, 64.05, 61.87, 55.08, and 43.53 mg g^{-1}, respectively. The corresponding removal percentages were 86.04%, 80.06%, 77.44%, 69.38%, and 54.42% after 60 min. The integration of GO into Sn-BDC-MOF resulted in a notable enhancement in both removal percentage and adsorption capacity. This improvement can be attributed to the increased number of adsorption sites and the strengthened interaction between the Sn-BDC-MOF/GO composite and Pb(II) ions.[49] However, it was observed that an excessive amount of GO led to pore blockage, thereby diminishing the composite's Pb(II) adsorption capacity. This finding is consistent with the results reported by Cao and his coauthors.[50,51] Consequently, the optimal composite ratio was determined to be 1MOF : 1GO.

3.2.4 Effect of initial concentration of Pb(II) and contact time. According to Fig. 5D, an increase in the concentration of Pb(II) up to 200 ppm results in a decrease in removal percentage values and an increase in adsorption capacity. This can be attributed to the abundance of empty adsorption sites on the surface of the Sn-BDC-MOF/GO composite, which causes a rapid increase in removal rate with increasing contact time.[52] With increasing contact time, the adsorption rate gradually decreases until equilibrium is achieved at 90 min. At this stage, the adsorption capacity increases from 76.03 to 161.14 mg g^{-1} as Pb(II) concentrations rise from 50 to 200 ppm. This enhancement is attributed to the stronger driving forces generated by elevated Pb(II) concentrations, facilitating the adsorption of Pb(II) ions onto the Sn-BDC-MOF/GO composite surface.[53] However, when Pb(II) concentrations reach 200 ppm, the adsorption sites on the composite become saturated, resulting in a significant decrease in removal efficiency from 95.05% to 40.89%.

3.3 Adsorption isotherm

Several isotherm models, including Langmuir, Freundlich, Temkin, and D–R, were employed to analyze the interaction between Sn-BDC-MOF/GO and Pb(II) ions. Table S1 presents the linear relationships for these models, while Fig. S2 displays the linearized graph. By comparing the R^2 values listed in Table 1, it was determined that the adsorption of Pb(II) onto Sn-BDC-MOF/GO was closely associated with Freundlich (0.995), Langmuir (0.993), and Temkin (0.996) models, rather than the D–R model (0.924). This indicates that both chemical and physical interactions play a role in the process.[54] Through examination, it has been determined that the Langmuir model's maximum adsorption capacity ($q_{\max,\text{cal}} = 200$ mg g^{-1}) aligns with the experimental value ($q_{\max,\text{exp}} = 197.44$ mg g^{-1}). Additionally, the R_L values presented in Table S2 fall between 0 and 1, indicating that the adsorption of Pb(II) onto the Sn-BDC-MOF/GO composite surface is a favorable process.[55] Additionally, the Freundlich constant ($n = 4.23$) demonstrates the strong adsorption suitability of Pb(II) ions onto the Sn-BDC-MOF/GO composite surface.[56] Additionally, the Temkin isotherm

Table 1 The parameters of the adsorption isotherm model for Pb(II) onto Sn-BDC-MOF/GO

Isotherm model	Parameters	Value
Langmuir	q_m (mg g^{-1})	200.0
	b (L mg^{-1})	0.155
	R^2	0.994
Freundlich	n	4.23
	k_F (L mg^{-1})	65.75
	R^2	0.996
Temkin	A (L g^{-1})	6.95
	B (J mol^{-1})	28.79
	b (kJ mol^{-1})	86.75
	R^2	0.996
D–R	q_s	168.78
	K_{ad} (mol^2 k^{-2} J^{-2})	8×10^{-7}
	E (kJ mol^{-1})	0.791
	R^2	0.924

indicated that the Pb(II) uptake process is predominantly governed by chemical interactions, as evidenced by the value of (b) being greater than 80 kJ mol^{-1}. Moreover, the binding energy (E) values from the (D–R) model, which are less than 8 kJ mol^{-1}, further confirm that the adsorption process is physical. Therefore, based on these isotherm models, the adsorption of lead ions onto the Sn-BDC-MOF/GO composite is characterized as a physicochemical process.[57,58]

3.4 Adsorption kinetics

Our study employed various kinetic models, including pseudo 1st order, pseudo 2nd order, and Elovich models, to elucidate the regulatory mechanism of Pb(II) adsorption onto the Sn-BDC-MOF/GO composite. The linear relationships of these models are detailed in Table S3. The results indicate that the pseudo-second-order model provides the most accurate explanation for Pb(II) adsorption, as evidenced by the superior R^2 values and the alignment between experimental (q_{exp}) and calculated (q_{cal}) adsorption capacities, as shown in Fig. S3 and Table 2. Additionally, the Elovich model supports our findings, demonstrating that the adsorption rate of Pb(II) surpasses the desorption rate, with α values exceeding β values.[59]

Table 2 The adsorption kinetic model parameters for the elimination of Pb(II) by Sn-BDC MOF/Composite

Kinetic models and parameters	Concentration (mg L^{-1}) 50	100	150	200
$q_{e,exp}$ (mg g^{-1})	76.03	143.75	170.56	190.90
Pseudo 1st order				
$q_{e,cal}$ (mg g^{-1})	70.33	167.33	181.27	208.51
K_1 (min^{-1})	0.043	0.054	0.048	0.049
R^2	0.988	0.966	0.984	0.978
Pseudo 2nd order				
$q_{e,cal}$ (mg g^{-1})	78.125	161.29	178.57	200
K_2 (g mg^{-1} min^{-1})	0.00088	0.00031	0.00029	0.00025
R^2	0.998	0.996	0.999	0.997
Elovich				
α (mg g^{-1} min^{-1})	31.595	79.582	88.903	104.023
β (mg g^{-1} min^{-1})	1.304	0.518	0.464	0.396
R^2	0.978	0.966	0.971	0.969

3.5 Adsorption thermodynamics

We conducted a thorough analysis of the impact of temperature on the adsorption of Pb(II) onto composite at varying temperatures (25, 35, 45, and 55 °C), using 5 mg of Sn-BDC-MOF/GO composite in 20 mL of Pb(II) solution of initial concentration 50 mg L^{-1} at pH = 6 for 60 min. In Fig. 6A, we observed a gradual decline in the adsorption capacity, from 69.12 to 54.30 mg g^{-1}, and removal percentage, from 86.41 to 67.86%, as the temperature rose from 25 to 55 °C. Our results reveal that the adsorption of Pb(II) onto the Sn-BDC-MOF/GO composite is an exothermic process and this consistent with prior research on GO and MOF-based adsorbents.[60,61] The decline in adsorption capacity with increasing temperature is also observed in Fig. 6B, which shows data for different time intervals. This decrease can be attributed to the weakening of attractive forces between the Sn-BDC-MOF/GO composite and lead ions, thereby reducing the efficiency of the adsorption process. Furthermore, at higher temperatures, the boundary layer's thickness decreases due to the increased tendency of lead ions to escape from the adsorbent surface into the solution phase, resulting in decreased adsorption.[62] To further investigate how temperature influences the adsorption behavior of Pb(II) onto the Sn-BDC-MOF/GO composite, we utilized the equations provided in Table S4, we were able to calculate the main thermodynamic parameters, which included ΔG^0, ΔH^0, and ΔS^0. Additionally, the Van't Hoff graph (Fig. 6C) enabled us to determine ΔS^0 and ΔH^0 through the intercept and slope of a line. Our findings indicate that Pb(II) adsorption onto the Sn-BDC-MOF/GO composite occurs in an orderly manner, as ΔS^0 is a negative value (−76.72 J mol^{-1} K^{-1}). Furthermore, as the K_c values decrease with increasing temperature and the ΔH^0 value is negative, the process is exothermic. It is important to note that the forces involved in the adsorption process significantly affect the magnitude of ΔH^0. If ΔH^0 ranges between 2-40 kJ mol^{-1}, it is attributed to dispersion forces, dipole–dipole forces (D.D), hydrogen bonding (H.B), and/or coordination exchange. On the other hand, if $\Delta H^0 > 60$ kJ mol^{-1}, it is attributed to chemical bond formation. In this study, the reported ΔH^0 value (−28.02 kJ mol^{-1}) indicates the existence of an exothermic physical adsorption process.[60] The negative ΔG^0 values that decreased from 298 to 328 K as shown in Table 3 indicated the spontaneity of the process.

3.6 Reusability

Having an adsorbent that can be reused and recycled is a cost-effective solution, as it decreases manufacturing expenses. The Sn-BDC-MOF/GO composite exhibited remarkable adsorption capabilities, sustaining a removal rate of more than 70% even after undergoing 6 cycles of adsorption and desorption, as illustrated in Fig. 7A. To further explore the reason behind the

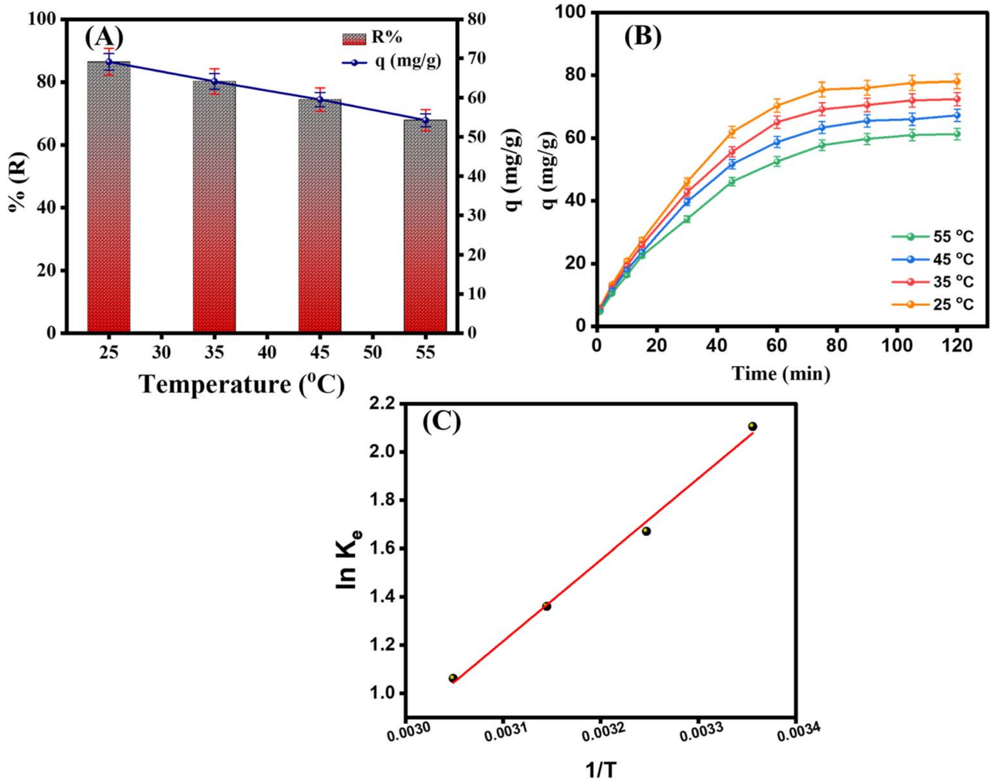

Fig. 6 (A) Effect of temperature on adsorption of Pb(II) onto Sn-BDC-MOF/GO at optimized condition (B) Adsorption capacity at different times and temperatures (C) Van't Hoff plot for removal of Pb(II) onto Sn-BDC-MOF/GO composite.

Table 3 Parameters of thermodynamics for adsorption of Pb(II) ions on Sn-BDC-MOF/GO composite

Temperature (K)	ΔG^0 (kJ mol^{-1})	ΔH^0 (kJ mol^{-1})	ΔS^0 (J mol^{-1} K^{-1})
298	−5.16	−28.02	−76.72
308	−4.39		
318	−3.62		
328	−2.86		

decline in Pb(II) removal efficiency after repeated use, post-cycling characterization was performed. The XRD pattern of the Sn-BDC-MOF/GO composite after six adsorption/desorption cycles (Fig. 7B) exhibited nearly identical peak positions to the composite before adsorption, with only a slight reduction in some peaks intensity. This indicates that the crystalline structure remained stable. Moreover, the SEM image after cycling (Fig. 7C) clearly shows that the rod-like Sn-BDC-MOF particles are still well dispersed over the crumpled GO sheets, maintaining the characteristic morphology observed before adsorption. Notably, the image also reveals the presence of fine white surface residues, which may correspond to retained Pb(II) ions that remained adsorbed despite regeneration. This visual evidence supports the hypothesis that strong interactions between Pb(II) and the composite's surface functional groups may limit complete desorption. Therefore, the observed decrease in adsorption performance is primarily attributed to partial blockage of the active sites by residual ions and their strong surface interactions, rather than material degradation.

3.7 Selectivity of composite

An experiment was conducted to evaluate the removal efficiency of Pb(II), Cu(II), and Cd(II) using 0.005 g of the Sn-BDC-MOF/GO composite. The experiment was carried out at an initial metal ion concentration of 50 ppm, a pH of 6, and a temperature of 25 °C. The results, as illustrated in Fig. 7D, demonstrated that the Sn-BDC-MOF/GO composite exhibited superior removal percentages and adsorption capacities for Pb(II) compared to Cu(II) and Cd(II). Specifically, the removal percentages for Pb(II), Cu(II), and Cd(II) were 85.16%, 77.64%, and 68.67%, respectively. The higher adsorption of Pb(II) ions compared to Cu(II) and Cd(II) can be attributed to several factors. Pb(II) ions have a higher electronegativity, which enhances their interaction with the adsorption sites on the Sn-BDC-MOF/GO composite. Additionally, the larger ionic radius of Pb(II) facilitates better interaction with surface functional groups such as hydroxyl (–OH) and carboxyl (–COOH) groups, Pb(II) ions are also more likely to form stable complexes with these functional groups, providing additional binding sites. The electrostatic attraction between the negatively charged sites on the composite and the positively charged Pb(II) ions is stronger, and Pb(II) has a higher chemical affinity for the adsorption sites, leading to more efficient adsorption. These factors collectively contribute to the superior adsorption capacity and removal efficiency of Pb(II)

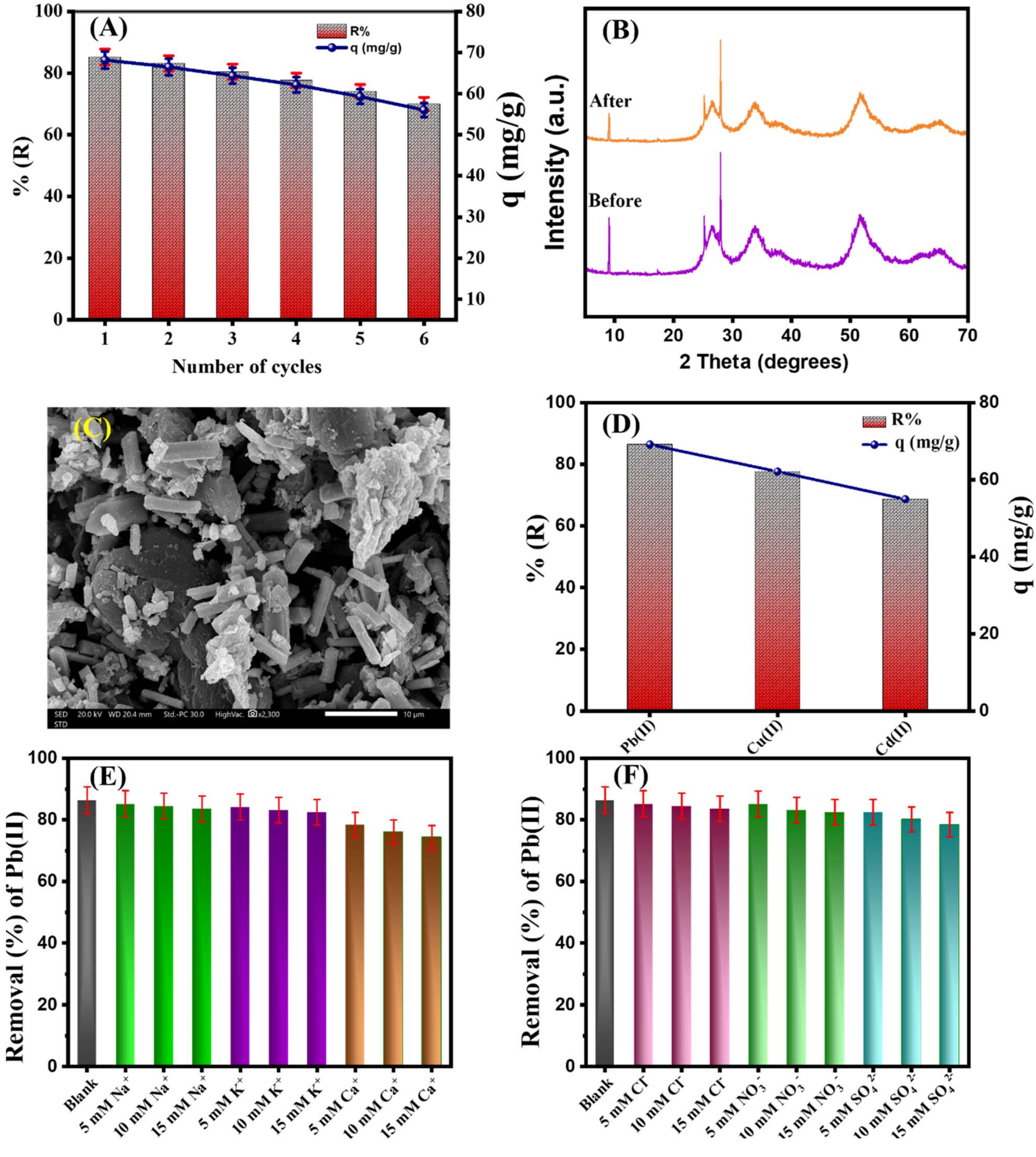

Fig. 7 (A) Reusability study, (B) XRD pattern of Sn-BDC-MOF/GO composite before and after six cycles of Pb(II) adsorption, (C) SEM of Sn-BDC-MOF/GO composite after six adsorption cycles, (D) Selectivity study, and The impact of interferance (E) cations and (F) anions on the Pb(II) adsorption.

ions.[63–65] To quantitatively assess the selectivity, the distribution coefficients (K_d) and relative selectivity factors (α) were calculated by utilizing equations provided in the Table S5. The K_d values for Pb(II), Cu(II), and Cd(II) were 6.36, 3.75, and 2.19 L g^{-1}, respectively, while the α were 1.83 for Pb(II)/Cu(II) and 2.90 for Pb(II)/Cd(II). These results confirm the high selectivity of the composite towards Pb(II)ions.

3.8 Interfering ions effect

Since wastewater typically contains a variety of ionic species, it is important to evaluate how these coexisting ions may interfere with Pb(II) adsorption onto the Sn-BDC-MOF/GO composite. To this end, individual tests were carried out in the presence of common cations (Na^+, K^+, and Ca^{2+}) and anions (Cl^-, NO_3^-, and SO_4^{2-}) at different concentrations. As shown in Fig. 7E, the

Table 4 Comparison of the maximum adsorption capacity of Sn-BDC-MOF/GO composite with other pertinent adsorbents for the Pb(II) removal

Adsorbent	Equilibration time	pH	$q_{\max}$ (mg g^{-1})	Reusability	Ref.
Fe_3O_4@BDC@AGPA	180 min	5.6	157	Efficiency after 5 cycles ~70%	68
Fe-BTC MOF	180 min	5.5	174	Efficiency after 3 cycles <70%	69
MMMT@Zn-BDC	90 min	6.5	175	Efficiency after 5 cycles ~80%	65
Fe_3O_4/UiO-66 NH_2@EDTA-GO	60 min	6	82.8	N/A	70
GO-COOH/MOF-808	20 min	5.5	157.8	Efficiency after 3 cycles <70%	71
GO-MLNPs	300 min	5	147.9	Efficiency after 5 cycles ~80%	72
GO-HBP-NH_2-CMC	120 min	6	152.9	N/A	73
MIL-101(Fe)/GO	15 min	6	128.6	Efficiency after 4 cycles ~80%	74
Cu(tpa). GO	120 min	6	35.1	N/A	75
Sn-BDC-MOF/GO	90 min	6	190.9	Efficiency after 6 cycles ~70%	This study

adsorption capacity of the composite remained almost unaffected by Na^+ and K^+. However, the introduction of Ca^{2+} reduced the Pb^{2+} removal efficiency, with the uptake decreasing to 73.8% at 15 mM. This pronounced competition can be ascribed to the higher charge density of Ca^{2+}, which improves its transport through the adsorption medium and enhances its interaction with the Sn-BDC-MOF/GO surface.[66] On the other hand, as depicted in Fig. 7F, neither Cl^- nor NO_3^- caused significant interference, while SO_4^{2-} considerably hindered Pb(II) removal, so the efficiency diminished to 78.7% at 15 mM due to its strong tendency to form both inner- and outer–sphere complexes with the composite surface.[67]

3.9 Comparison study

A comparison study was conducted to evaluate the adsorption performance of the synthesized Sn-BDC-MOF/GO composite against other MOF-based Pb(II) sorbents recently reported in the literature (Table 4). The Sn-BDC-MOF/GO composite exhibited outstanding adsorption performance, outperforming several MOF/GO hybrids. The remarkable adsorption capacity ($q_{\max}$ = 190.90 mg g^{-1}) can be attributed to the synergistic interaction between the Sn-BDC-MOF framework and graphene oxide sheets, which provide abundant adsorption sites and facilitate Pb(II) ion diffusion. In addition, the composite demonstrated rapid adsorption kinetics and excellent reusability over several cycles, underscoring its potential as a high-performance sorbent for Pb(II) removal.

3.10 DFT calculations

Assessing the reactivity of a molecule and the progression of chemical reactions relies on identifying the geometry of the Frontier orbitals.[76] When the metal ion's LUMO is closer to the

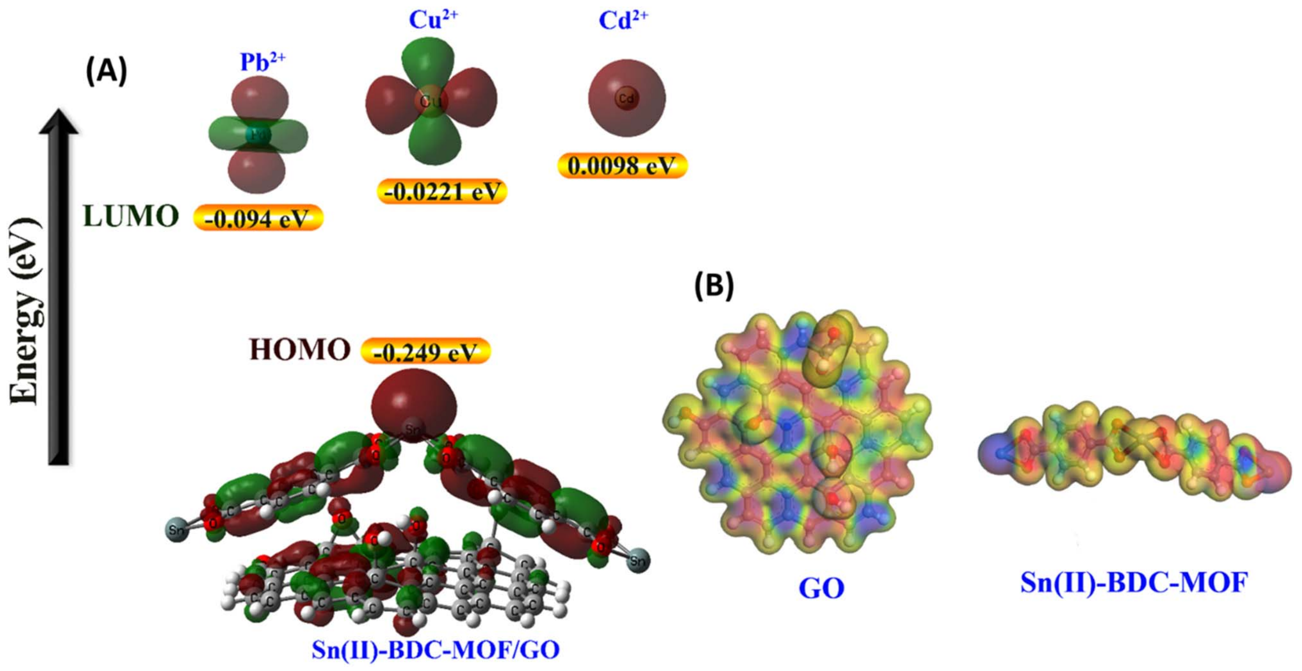

Fig. 8 (A). HOMO and LUMO surfaces for Sn-BDC-MOF/GO composite and metal ions and (B) MEP for GO and Sn-BDC-MOF.

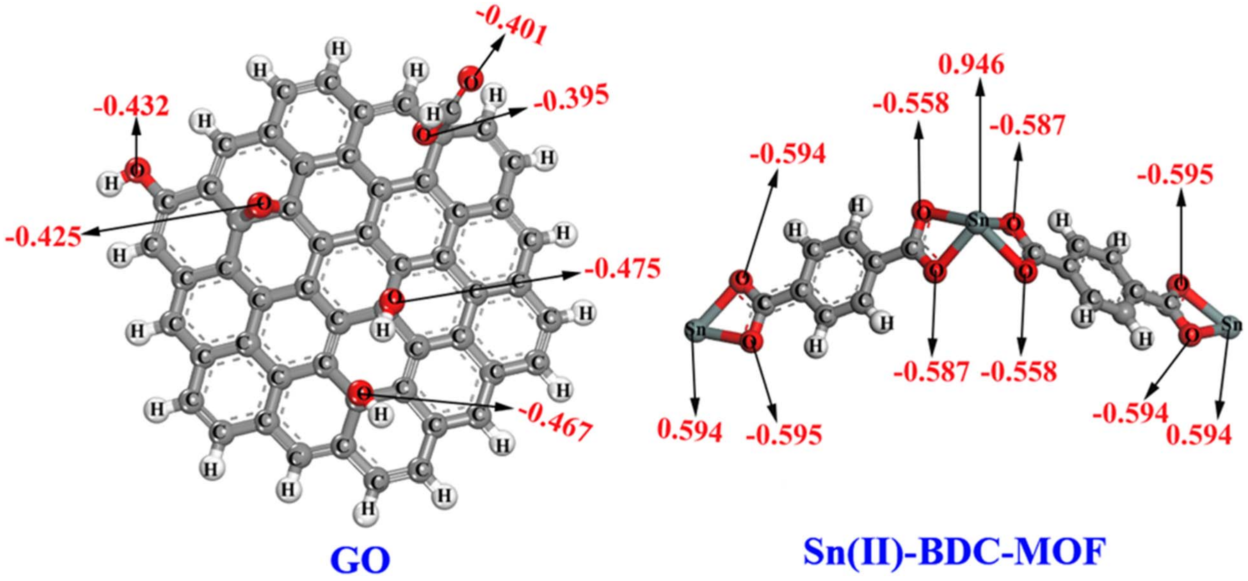

Fig. 9 The optimized structures of GO and Sn-BDC-MOF with the highest values of the Mulliken atomic (MAC).

Sn-BDC-MOF/GO composite's HOMO, the net charge on the metal ion increases due to the Sn-BDC-MOF/GO composite's contribution.[77] In order to transfer charge from the composite to the metal ions and increase the strength of adsorption, the filled orbitals localized on Sn-BDC-MOF/GO composite and the vacant d-orbitals on metal ions overlap.[78] The HOMO of the Sn-BDC-MOF/GO composite and the LUMO of the metal ion must be compared in order to determine which ions are more easily adsorbed. Fig. 8A shows that the order of LUMO of metal ions is Cd(II) > Cu(II) > Pb(II), so the LUMO of Pb(II) is the closest to the HOMO of composite. This indicates that lead was adsorbed in greater quantity, and the predictable order of adsorption is as follows: Pb(II) > Cu(II) > Cd(II). However, it is important to note that frontier orbitals are not the sole factor in understanding the adsorption process; adsorption energy must also be considered.

In Fig. 8B, the Molecular Electrostatic Potential (MEP) maps of Sn-BDC-MOF and GO are presented. These maps use color coding to indicate the distribution of electrostatic potential across the molecules, where red regions signify areas of higher negative charge, and blue regions indicate areas of higher positive charge.[79] The MEP analysis reveals that the oxygen atoms in both Sn-BDC-MOF and GO exhibit the highest negative charges, which suggests a high electron density around these atoms. This high electron density enhances their ability to interact with metal ions, facilitating the formation of coordinate bonds between the metal ions and the oxygen atoms. This assertion is further supported by the Mulliken atomic charges (MAC) analysis shown in Fig. 9, which quantifies the distribution of electronic charge among the atoms in the molecules.

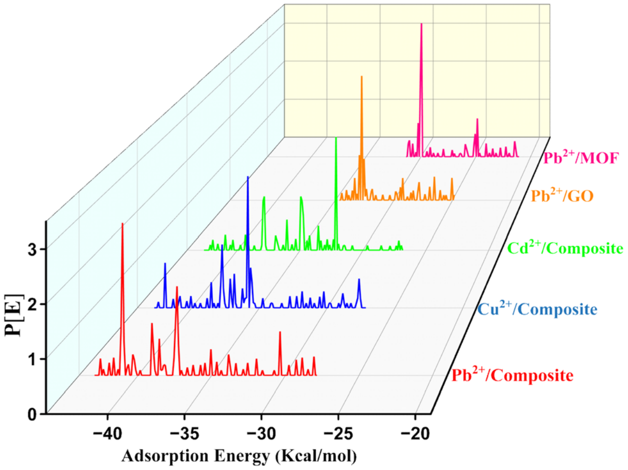

Fig. 10 Shows the distribution of adsorption energies for various adsorptive configurations of Pb(II), Cu(II), and Cd(II).

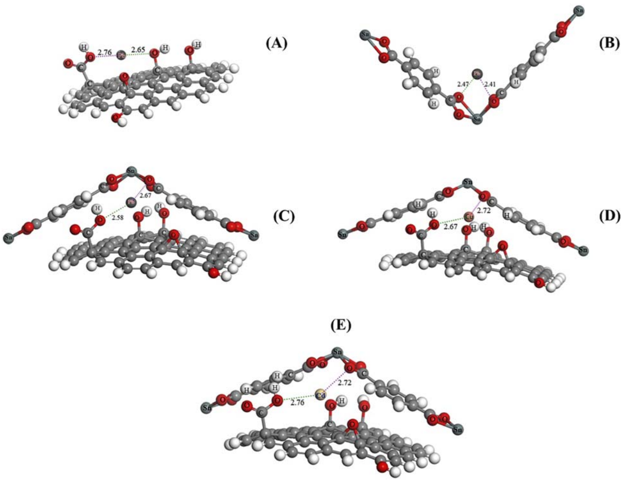

Fig. 11 The optimized structures of adsorption for (A) Pb(II) onto GO, (B) Pb(II) onto Sn-BDC-MOF (C) Pb(II) onto composite, (D) Cu(II) onto composite, and (E) Cd(II) onto composite.

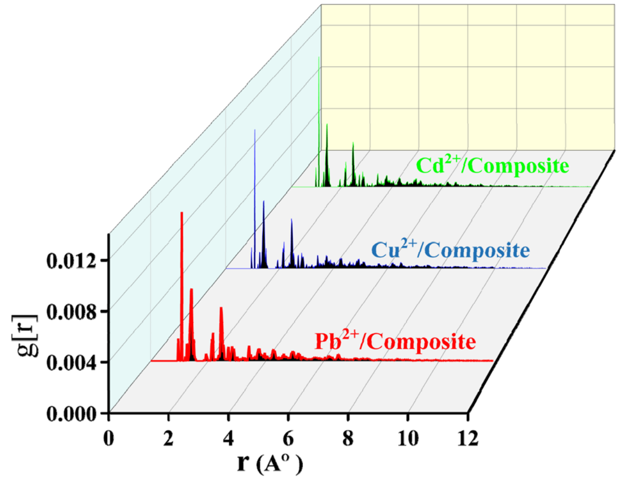

Fig. 12 Radial Distribution Function (RDF) for Pb(II), Cu(II), and Cd(II) ions on the Sn-BDC-MOF/GO composite surface.

The MAC data confirm that the oxygen atoms possess the highest negative charges, reinforcing the conclusion drawn from the MEP analysis. The strong interaction between the negatively charged oxygen atoms and the positively charged metal ions underscores the significant role of oxygen in the adsorption process, making it a critical factor in the efficiency of metal ion removal by the Sn-BDC-MOF/GO composite.

The adsorption energy between metal ions and the surface of the Sn-BDC-MOF/GO composite can be calculated using the following equation:

$$E_{\text{adsorption}} = E_{\text{composite/M}}{}^{n+} - (E_{\text{composite}} + E_{\text{M}}{}^{n+})$$

where $E_{\text{composite/M}}{}^{n+}$ is the total energy of the simulated system, $E_{\text{composite}}$ and $E_{\text{M}}{}^{n+}$ are the total calculated energy of the Sn-BDC-MOF/GO composite surface and that of the free metal ion has charge (n), respectively.

The adsorption energies (E_{ads}) for each ion are as follows: Pb(II) ranges from −28.02 to −42.57 kcal mol^{-1} (with a maximum E_{ads} of −41.05 kcal mol^{-1}), Cu(II) ranges from −26.83 to −42.68 kcal mol^{-1} (with a maximum E_{ads} of −35.85 kcal mol^{-1}), and Cd(II) ranges from −24.88 to −42.12 kcal mol^{-1} (with a maximum E_{ads} of −32.15 kcal mol^{-1}) as shown in Fig. 10. These values were experimentally confirmed, indicating that Pb(II) had the highest adsorption energy, followed by Cu(II) and then Cd(II). The high E_{ads} values suggest a strong interaction between the metal ions and the composite surface. Additionally, the E_{ads} values showed that Pb(II) adsorbed more strongly onto the composite surface compared to GO and MOF.[80] The bond length in Fig. 11 also support this conclusion, demonstrating a strong interaction between the metal ions and the composite surface.[81]

Based on the analysis of the Radial Distribution Function (RDF) shown in Fig. 12, it can be concluded that chemisorption occurs at 1 to 3.5 Å from the composite surface, as evidenced by the peak in the RDF graph. On the other hand, physisorption is indicated by the appearance of RDF peaks at distances greater than 3.5 Å.[82] The RDF measurements for Pb(II), Cu(II), and Cd(II) were found to be below 3.5 Å. Subsequent analysis of the adsorption energy and corresponding RDF data provided

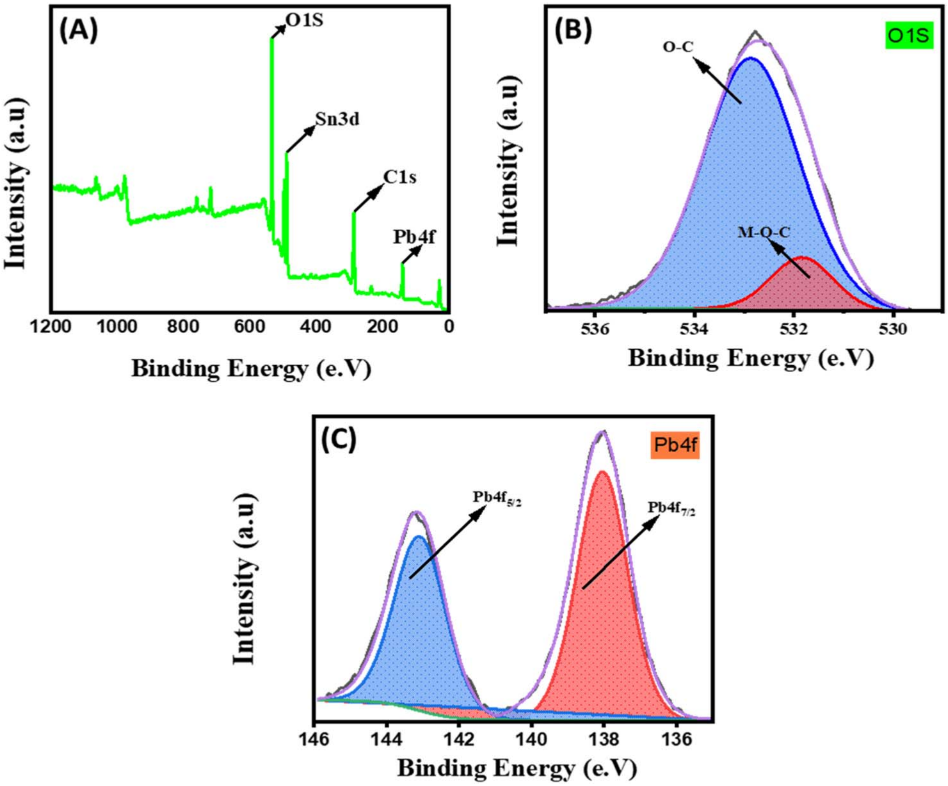

Fig. 13 XPS of Sn-BDC-MOF/GO composite after adsorption: (A) wide spectra, (B) Pb 4f, and (C) O 1s.

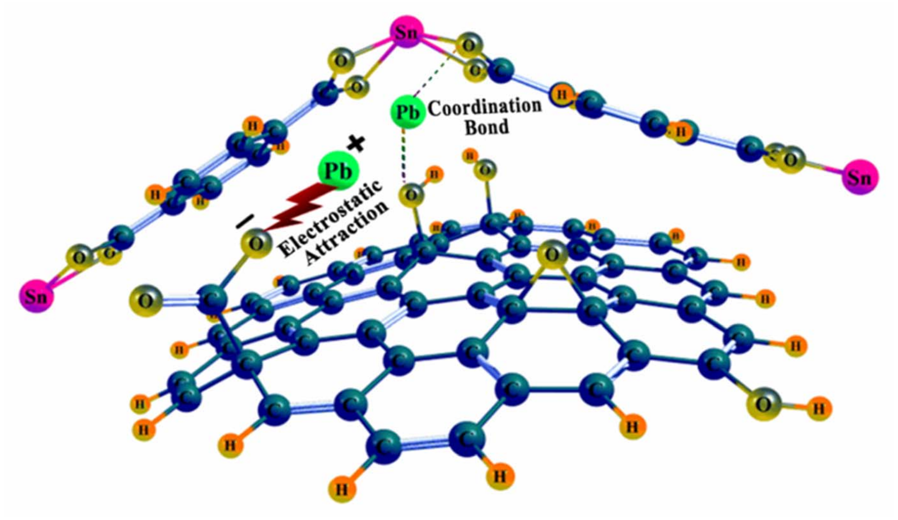

Fig. 14 A schematic representation for the adsorption mechanism of Pb(II) on Sn-BDC-MOF/GO.

confirmation that the metal ions have a strong affinity for adhering to the composite surface, thereby rendering it a highly efficient agent for the removal of these ions from water.

3.11 Mechanism of adsorption

In Fig. 13A, XPS measurements were conducted to analyze how Pb(II) interacts with Sn-BDC-MOF/Composite after adsorption. A comparison was made between the composite before and after adsorption, which revealed a new peak (Pb 4f). This peak was further divided into two peaks, Pb $4f_{7/2}$ (137.99 eV) and Pb $4f_{5/2}$ (143.09 eV), indicating successful adsorption of Pb(II)as show in Fig. 13B. This is in contrast to the binding energy of pure $Pb(NO_3)_2$, where the $4f_{5/2} = 144.5$ eV and $4f_{7/2} = 139.6$ eV peaks shifted to a lower energy band due to the interaction between Pb ions and the composite. Notable changes were observed in the oxygen atom environment, with the C–O–M peak intensity decreasing and shifting towards lower energy (531.83 eV), indicating the formation of the C–O–Pd bond as shown in Fig. 13C. Additionally, the C–O peak intensity increased and shifted to lower energy (532.86 eV). These findings suggest that the adsorption of Pb(II) ions takes place mainly through chemical interaction *via* complexation with the oxygen groups on the composite surface. Zeta potential measurements showed that the Sn-BDC-MOF/GO composite surface carries a high negative charge (−25.8 mV) at pH = 6, indicating strong electrostatic interactions between the composite surface and Pb(II). Theoretical calculations support that the adsorption of Pb(II) occurs through chemical adsorption onto the composite surface *via* donor/acceptor interaction between the free electrons of (O) and the vacant d-orbital of the Pb ions. Finally, the adsorption mechanism presented in Fig. 14.

4 Conclusion

We have developed and tested a new composite material, named Sn-BDC-MOF/GO, for its efficacy in removing Pb(II) ions. Results from batch adsorption mode demonstrated that the composite material was significantly more effective in removing Pb(II) ions than Sn-BDC-MOF alone. The data revealed that the process followed both Langmuir and Freundlich isotherms, and the adsorbent's maximum adsorption capacity was found to be 200 mg g^{-1} at pH = 6. The adsorption process was exothermic and followed the pseudo-second order kinetic model. The composite material was also reusable, with removal efficiency as high as 70% after six consecutive cycles, while maintaining good selectivity in actual wastewater. Although XPS data and DFT calculations, it was found that electrostatic interaction and coordination were the main mechanisms in the adsorption process. This novel Sn-BDC-MOF/GO adsorbent holds great promise for future applications in heavy metal removal.

Conflicts of interest

The authors declare no competing interests.

Data availability

The data sets used and analyzed during the current study are available from the corresponding author on reasonable request.

Supplementary information is available. See DOI: **https://doi.org/10.1039/d5ra04912a**.

References

1 E. M. A. El-Monaem, M. M. A. El-Latif, A. S. Eltaweil and G. M. El-Subruiti, *Nano*, 2021, **16**, 2150039.
2 A. A. Mitiku, *Int. J. Pharm. Sci. Rev. Res.*, 2020, **60**, 94–101.
3 A. M. Omer, G. S. Elgarhy, G. M. El-Subruiti, E. M. Abd El-Monaem and A. S. Eltaweil, *Carbohydr. Polym.*, 2023, **311**, 120771.
4 D. Kapoor and M. P. Singh, in *Heavy Metals in the Environment*, Elsevier, 2021, pp. 179–189.

5 Z. Rahman and V. P. Singh, *Environ. Monit. Assess.*, 2019, **191**, 1–21.

6 A. Ara and J. A. Usmani, *Interdiscip. Toxicol.*, 2015, **8**, 55–64.

7 P. Levallois, P. Barn, M. Valcke, D. Gauvin and T. Kosatsky, *Curr. Environ. Health Rep.*, 2018, **5**, 255–262.

8 S. Hernberg, *Am. J. Ind. Med.*, 2000, **38**, 244–254.

9 M. R. Lasheen, N. S. Ammar and H. S. Ibrahim, *Solid State Sci.*, 2012, **14**, 202–210.

10 V. K. Gupta, R. Kumar, A. Nayak, T. A. Saleh and M. Barakat, *Adv. Colloid Interface Sci.*, 2013, **193**, 24–34.

11 M. T. Yagub, T. K. Sen, S. Afroze and H. M. Ang, *Adv. Colloid Interface Sci.*, 2014, **209**, 172–184.

12 F. A. Elaiwi and A. Sirkecioglu, *Sep. Sci. Technol.*, 2020, **55**, 3362–3374.

13 E. M. Abd El-Monaem, A. M. Omer and A. S. Eltaweil, *J. Polym. Environ.*, 2024, **32**, 2075–2090.

14 Y. Pi, X. Li, Q. Xia, J. Wu, Y. Li, J. Xiao and Z. Li, *Chem. Eng. J.*, 2018, **337**, 351–371.

15 K. Sumida, D. L. Rogow, J. A. Mason, T. M. McDonald, E. D. Bloch, Z. R. Herm, T.-H. Bae and J. R. Long, *Chem. Rev.*, 2012, **112**, 724–781.

16 R. Ricco, K. Konstas, M. J. Styles, J. J. Richardson, R. Babarao, K. Suzuki, P. Scopece and P. Falcaro, *J. Mater. Chem. A*, 2015, **3**, 19822–19831.

17 A. Aijaz, A. Karkamkar, Y. J. Choi, N. Tsumori, E. Rönnebro, T. Autrey, H. Shioyama and Q. Xu, *J. Am. Chem. Soc.*, 2012, **134**, 13926–13929.

18 E. M. Abd El-Monaem, M. Hosny and A. S. Eltaweil, *Chem. Eng. Sci.*, 2024, **287**, 119707.

19 P. Horcajada, R. Gref, T. Baati, P. K. Allan, G. Maurin, P. Couvreur, G. Férey, R. E. Morris and C. Serre, *Chem. Rev.*, 2012, **112**, 1232–1268.

20 J. Gu, L. Sun, Y. Zhang, Q. Zhang, X. Li, H. Si, Y. Shi, C. Sun, Y. Gong and Y. Zhang, *Chem. Eng. J.*, 2020, **385**, 123454.

21 W. Lu, X. Guo, Y. Luo, Q. Li, R. Zhu and H. Pang, *Chem. Eng. J.*, 2019, **355**, 208–237.

22 J.-Z. Gu, W.-G. Lu, L. Jiang, H.-C. Zhou and T.-B. Lu, *Inorg. Chem.*, 2007, **46**, 5835–5837.

23 S. Thangavel and G. Venugopal, *Powder Technol.*, 2014, **257**, 141–148.

24 H. Luo, F. Feng, F. Yao, Y. Zhu, Z. Yang and Y. Wan, *J. Nanosci. Nanotechnol.*, 2020, **20**, 719–730.

25 A. S. Eltaweil, H. M. Elshishini, Z. F. Ghatass and G. M. Elsubruiti, *Powder Technol.*, 2021, **379**, 407–416.

26 B. Szczęśniak, J. Choma and M. Jaroniec, *J. Colloid Interface Sci.*, 2018, **514**, 801–813.

27 X. Yue, T. Zhang, D. Yang, F. Qiu and Z. Li, *J. Cleaner Prod.*, 2018, **199**, 411–419.

28 Z.-h. Zhang, J.-l. Zhang, J.-m. Liu, Z.-h. Xiong and X. Chen, *Water, Air, Soil Pollut.*, 2016, **227**, 1–12.

29 J. Zhang and L. Gao, *J. Solid State Chem.*, 2004, **177**, 1425–1430.

30 K. C. Song and Y. Kang, *Mater. Lett.*, 2000, **42**, 283–289.

31 A. Ghosh and G. Das, *Microporous Mesoporous Mater.*, 2020, **297**, 110039.

32 N. Brainer, T. dos Santos, C. D. Barbosa and S. Meneghetti, *Mater. Lett.*, 2020, **280**, 128512.

33 A. S. Eltaweil, G. S. Elgarhy, G. M. El-Subruiti and A. M. Omer, *Int. J. Biol. Macromol.*, 2020, **154**, 307–318.

34 A. S. Eltaweil, E. M. Abd El-Monaem, G. M. El-Subruiti, B. M. Ali, M. M. Abd El-Latif and A. M. Omer, *J. Porous Mater.*, 2023, **30**, 607–618.

35 T. K. Vo, N. H. Y. Phuong, V. C. Nguyen and D. T. Quang, *Chemosphere*, 2023, **341**, 139996.

36 H. A. L. Pham, T. K. Vo, D. T. Nguyen, H. K. Huynh, Q. T. S. Pham and V. C. Nguyen, *Green Chem. Lett. Rev.*, 2022, **15**, 572–581.

37 T. M. N. Bui, T. K. Vo, N. H. Y. Phuong, V. H. Nguyen, V. C. Nguyen, Q. H. Nguyen and N. T. T. Dang, *Sep. Purif. Technol.*, 2025, **355**, 129723.

38 T. K. Vo, J. Kim, J. Park, D. Q. Dao and H. B. Truong, *Chem. Eng. J.*, 2024, **481**, 148570.

39 T. H. A. Nguyen, P. Van Hung, H. L. Tran, M. Q. Nguyen, V. T. Khue and T. K. Vo, *Colloids Surf., A*, 2025, **710**, 136296.

40 E. M. Abd El-Monaem, M. S. Ayoup, A. M. Omer, E. N. Hammad and A. S. Eltaweil, *Appl. Water Sci.*, 2023, **13**, 67.

41 G. Jnido, G. Ohms and W. Viöl, *Coatings*, 2021, **11**, 183.

42 D. V. Sivkov, O. V. Petrova, S. V. Nekipelov, A. S. Vinogradov, R. N. Skandakov, K. A. Bakina, S. I. Isaenko, A. M. Ob'edkov, B. S. Kaverin and I. V. Vilkov, *Appl. Sci.*, 2022, **12**, 7744.

43 J. Rani, J. Lim, J. Oh, D. Kim, D. Lee, J.-W. Kim, H. S. Shin, J. H. Kim and S. C. Jun, *RSC Adv.*, 2013, **3**, 5926–5936.

44 D. N. Dirin, A. Wieczorek, S. Siol, M. V. Kovalenko and M. I. Bodnarchuk, *Nano Lett.*, 2025, **25**(29), 11187–11190.

45 P. Sun, L. You, Y. Sun, N. Chen, X. Li, H. Sun, J. Ma and G. Lu, *CrystEngComm*, 2012, **14**, 1701–1708.

46 C. Bielawski, D. Dreyer, S. Park and R. Ruoff, *Chem. Soc. Rev.*, 2010, **39**, 228–240.

47 N. Feng, X. Guo, S. Liang, Y. Zhu and J. Liu, *J. Hazard. Mater.*, 2011, **185**, 49–54.

48 F. Ren, Z. Li, W.-Z. Tan, X.-H. Liu, Z.-F. Sun, P.-G. Ren and D.-X. Yan, *J. Colloid Interface Sci.*, 2018, **532**, 58–67.

49 B. Chen, Y. Li, M. Li, M. Cui, W. Xu, L. Li, Y. Sun, M. Wang, Y. Zhang and K. Chen, *Microporous Mesoporous Mater.*, 2021, **328**, 111457.

50 Y. Cao, Y. Zhao, Z. Lv, F. Song and Q. Zhong, *J. Ind. Eng. Chem.*, 2015, **27**, 102–107.

51 Z. Liu, W. He, Q. Zhang, H. Shapour and M. F. Bakhtari, *ACS Omega*, 2021, **6**, 4597–4608.

52 J. Potgieter, S. Potgieter-Vermaak and P. Kalibantonga, *Miner. Eng.*, 2006, **19**, 463–470.

53 N. Elboughdiri, *Cem. Eng.*, 2020, **7**, 1782623.

54 H. Gomaa, A. Sayed, M. Mahross, M. Abdel-Hakim, I. M. Othman, J. Li and S. M. El-Bahy, *Microporous Mesoporous Mater.*, 2022, **330**, 111578.

55 A. B. D. Nandiyanto, G. C. S. Girsang, R. Maryanti, R. Ragadhita, S. Anggraeni, F. M. Fauzi, P. Sakinah, A. P. Astuti, D. Usdiyana and M. Fiandini, *Commun. Sci. Technol.*, 2020, **5**, 31–39.

56 A. S. Eltaweil, O. A. Hashem, H. Abdel-Hamid, E. M. Abd El-Monaem and M. S. Ayoup, *Int. J. Biol. Macromol.*, 2022, **222**, 1465–1475.

57 V. Puccia and M. J. Avena, *Colloid Interface Sci. Commun.*, 2021, **41**, 100376.
58 G. S. dos Reis, S. H. Larsson, M. Thyrel, T. N. Pham, E. Claudio Lima, H. P. de Oliveira and G. L. Dotto, *Coatings*, 2021, **11**, 772.
59 R.-L. Tseng, H. N. Tran and R.-S. Juang, *J. Taiwan Inst. Chem. Eng.*, 2022, **136**, 104403.
60 Y. Li, Q. Du, T. Liu, J. Sun, Y. Wang, S. Wu, Z. Wang, Y. Xia and L. Xia, *Carbohydr. Polym.*, 2013, **95**, 501–507.
61 E. Yılmaz, E. Sert and F. S. Atalay, *J. Taiwan Inst. Chem. Eng.*, 2016, **65**, 323–330.
62 R. Singh and R. Bhateria, *ACS Omega*, 2020, **5**, 10826–10837.
63 R. Sitko, E. Turek, B. Zawisza, E. Malicka, E. Talik, J. Heimann, A. Gagor, B. Feist and R. Wrzalik, *Dalton Trans.*, 2013, **42**, 5682–5689.
64 J. Shen, X. Xu, X.-k. Ouyang and M.-c. Jin, *J. Polym. Environ.*, 2022, 1–12.
65 J. Shen, N. Wang, Y. G. Wang, D. Yu and X. k. Ouyang, *Polymers*, 2018, **10**, 1383.
66 R. Li, Y. Liu, G. Lan, H. Qiu, B. Xu, Q. Xu, N. Sun and L. Zhang, *J. Environ. Chem. Eng.*, 2021, **9**, 105310.
67 X. Lin, G. Wei, X. Liang, J. Liu, L. Ma and J. Zhu, *Minerals*, 2021, **11**, 88.
68 M. Alsuhybani, A. Alshahrani, M. Algamdi, A. A. Al-Kahtani and A. A. Alqadami, *J. Mol. Liq.*, 2020, **301**, 112393.
69 A. Castañeda-Ramírez, E. Rojas-García, R. López-Medina, D. García-Martínez, J. Nicolás-Antúnez and A. Maubert-Franco, *Catal. Today*, 2022, **394**, 94–102.
70 M. Cao and W. Yang, *React. Chem. Eng.*, 2024, **9**, 317–338.
71 Z. Xie, S. Diao, R. Xu, G. Wei, J. Wen, G. Hu, T. Tang, L. Jiang, X. Li and M. Li, *Appl. Surf. Sci.*, 2023, **636**, 157827.
72 B. Du, L. Chai, W. Li, X. Wang, X. Chen, J. Zhou and R.-C. Sun, *Sep. Purif. Technol.*, 2022, **297**, 121509.
73 Q. Kong, S. Preis, L. Li, P. Luo, Y. Hu and C. Wei, *Int. J. Biol. Macromol.*, 2020, **149**, 581–592.
74 M. Lu, L. Li, S. Shen, D. Chen and W. Han, *New J. Chem.*, 2019, **43**, 1032–1037.
75 E. Rahimi and N. Mohaghegh, *Environ. Sci. Pollut. Res.*, 2017, **24**, 22353–22360.
76 A. Berisha, F. Podvorica, V. Mehmeti, F. Syla and D. Vataj, *Maced. J. Chem. Chem. Eng.*, 2015, **34**, 287–294.
77 A. Paredes-Doig, A. Pinedo-Flores, J. Aylas-Orejón, D. Obregón-Valencia and M. Sun Kou, *Adsorpt. Sci. Technol.*, 2020, **38**, 191–204.
78 A. L. Paredes-Doig, M. d. R. Sun-Kou, G. Picasso-Escobar and J. L. Cannata, *Adsorpt. Sci. Technol.*, 2014, **32**, 165–180.
79 L. Ouksel, R. Bourzami, N. Hamdouni and A. Boudjada, *J. Mol. Struct.*, 2021, **1229**, 129792.
80 A. Berisha, *Electrochem*, 2020, **1**, 188–199.
81 Q. Kong, S. Preis, L. Li, P. Luo, C. Wei, Z. Li, Y. Hu and C. Wei, *Sep. Purif. Technol.*, 2020, **232**, 115956.
82 A. A. Al-Amiery, A. A. H. Kadhum, A. Kadihum, A. B. Mohamad, C. K. How and S. Junaedi, *Materials*, 2014, **7**, 787–804.